Numerical and experimental investigations on the buckling of steel semi-spherical shells under various loadings

M. Shariati *, H.R. Allahbakhsh

Mechanical Department, Shahrood University of Technology, Shahrood, Iran

ABSTRACT

In this paper, the buckling and post-buckling of steel thin-walled semi-spherical shells are investigated under different loadings, both experimentally and numerically. Various vertical compression loadings are applied to specimens using the following methods: a rigid flat plate and some rigid bars with circular, square and spherical cross sections, a rigid tube, a plate with a hole, and an indented tube. The effects of geometrical parameters of specimens on the buckling load, such as the diameter and thickness, are studied. The numerical analysis is carried out by ABAQUS software and the experimental tests are performed using an Instron 8802 servo-hydraulic machine. The numerical and experimental results are similar to one another. Therefore, the numerical results are valid.

1. Introduction

Thin-walled semi-spherical shells are often used in structures due to their energy-absorbing capacity. The buckling behavior of these shells gives rise to their critical design applications, including the automobile bodies, aircraft fuselages, and ship hulls.

The large deformation of a thin-walled sphere or a spherical shell, known as a typical post-buckling problem, has received attention since the 1960s. Leckie and Penny [1] performed a series of tests on carefully manufactured hemispherical shells that were loaded centrally by a rigid bar. These experiments were followed by a theoretical study of Morris and Calladine [2]. The authors reached a new milestone in understanding the crushing behavior of revolving shells. Their studies shows that plastic deformation is indeed confined to a relatively narrow ring or section of a toroidal surface, and that the ring is moving outward as the deformation processes.

Updike [3] first studied the major deformation of rigid plastic semi-spherical shells compressed between two rigid plates. From his research, he proposed an analytical model. The computation was restricted to compressions that were less than or equal to approximately $\frac{1}{10}$th of the shells radius. Kitching et al. [4] studied deformation patterns on semi-spherical shells with R/t ratios between 36 and 420 experimentally and analytically. De'Oliveria

and Wierzbicki [5] conducted the same study. They completed a crushing analysis of rotationally symmetric plastic shells. Kinkead et al. [6] completed a quasi-static study on semi-spherical shells with R/t ratios between 36 and 420. This study produced similar results as previous studies. Gupta et al. [7] performed experiments on metallic semi-spherical shells with R/t ratios ranging between 15 and 240. Gupta et al. [7] examined three levels of deformation: local flattening, inward dimpling, and multiple lobes. Gupta and Venkatesh [8] presented a two-dimensional numerical analysis for semi-spherical shells under axial impact. In this study, a strong correlation was observed between the numerical simulation and the experimental results in buckling behavior that are related to the first mode jumping from local flattening to inward dimpling. In another study presented by Gupta and Gupta [9], the semi-spherical shells of R/t ratios between 26 and 45 had similar results when they were analyzed experimentally and computationally. In these experiments, all of the spherical shells were found to collapse in an axisymmetric mode. Ruan et al. [10] performed a series of tests on a ping-pong ball loaded by a rigid plate, rigid bar, and a rigid tube. He conducted these tests to explore the various post-bucking behaviors of a spherical shell and to compare the results with existing theoretical models proposed by Morris and Calladine [2], Updike [3] and De'Olivier and Wierzbicki [5].

The main purpose for the majority of investigations is to study the high-energy absorption of shells. The amount of energy absorbed is a function of the method of application of loads, transmission rates, deformation or displacement patterns, and material properties [11]. With the exception of loading by rigid

* Corresponding author.
E-mail addresses: mshariati@shahroodut.ac.ir, mshariati44@gmail.com
(M. Shariati).

plate, a literature search revealed minimal documentation of the response of the buckling and energy absorption of semi-spherical to various loading. It is noteworthy, that the mean collapse load can occur in higher and controllable levels with change of the method of application of loads. In this paper, a linear and a nonlinear analysis were conducted to study the effect of the method of application of loads on the buckling and post-buckling behavior on semi-spherical shells. Various vertical compression loadings are applied to specimens and the mean collapse load are obtained for each other. The ABAQUS finite element software was used. Semi-spherical shells with R/t ratios between 22 and 72 were analyzed. Several buckling tests were performed using an INSTRON 8802 servo-hydraulic machine. The results were compared with the results of the finite element method. A strong correlation between experiments and numerical simulations was observed.

2. Numerical analysis using the finite element method

The numerical simulations were carried out using the finite element software ABAQUS 6.7-1.

2.1. Geometry and mechanical properties of the shells

In this study, thin-walled semi-spherical shells with three different diameters ($L=102$, 77, 53 mm) and four different thicknesses ($t=0.7$, 0.8, 1.0, 1.2 mm) were analyzed. Fig. 1 shows the geometry of the specimens. According to Fig. 1, parameters (D, d, t, h) show the upper diameter, lower diameter, thickness, and height of the semi-spherical shells, respectively.

Specimens were nominated as follows: $D102–d25–t0.8–h38$. The numbers following D, d, t, and h quantify these dimensions for the specimen.

The semi-spherical shells used for this study were made of a mild steel alloy. The mechanical properties of the steel alloy were determined according to the ASTM E8 standard [12], using the INSTRON 8802 servo-hydraulic machine. Fig. 2 shows the stress–strain curve. Based on the linear portion of the stress–strain curve, the value of the elasticity module was computed as $E=150$ GPa and the value of yield stress was obtained as $\sigma=404$ MPa.
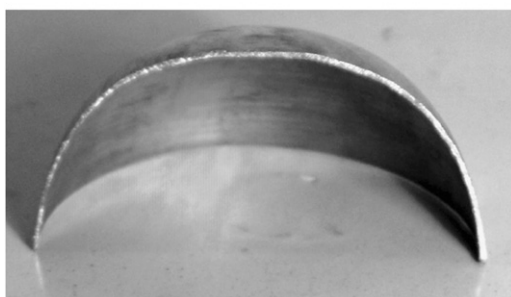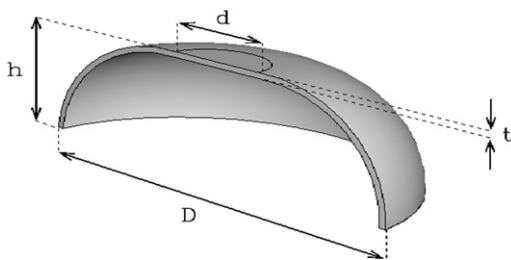
Furthermore, the value of Poisson's ratio was assumed to be $v=0.33$.

2.2. Boundary conditions

To apply boundary conditions to the bottom edges of the semi-spherical shells, a rigid plate was attached to the bottom edges of the semi-spherical shells. To analyze their buckling numerically, the specimens were subjected to an axial load similar to the load in the experimental tests. In this process, a displacement was applied to the center of the upper plate, bar, or tube.

With the exception of the longitudinal axis direction, all degrees of freedom in the lower plate and in the upper plate, bar, or tube were constrained.

2.3. Element formulation of the specimens

For this analysis, the nonlinear element, S8R5, was an eight-node element with six degrees of freedom per node and was suitable for the analysis of thin shells. The linear element, S4R, was a four-node element. Both linear and nonlinear elements were used for the analysis of the shells. These results were compared with each other. For the rigid plate, bar, or tube, the element R3D4 was used. A friction coefficient of 0.1 was recorded. The effect of the friction coefficient ranged from 0.08 to 0.12 and affected results by less than 1% [8].

2.4. Numerical process

In this study, an eigenvalue analysis overestimates the value of the buckling load because the plastic properties of the material do not have any role in the analyses procedure [13]. An initial eigenvalue analysis should be conducted for all specimens of a buckling analysis in order to find the mode shapes and corresponding eigenvalues. The first modes have smaller eigenvalues and buckling usually occurs in these mode shapes. For an eigenvalues analysis, the "buckle" step was completed by ABAQUS. For all specimens, three first-mode shapes and their
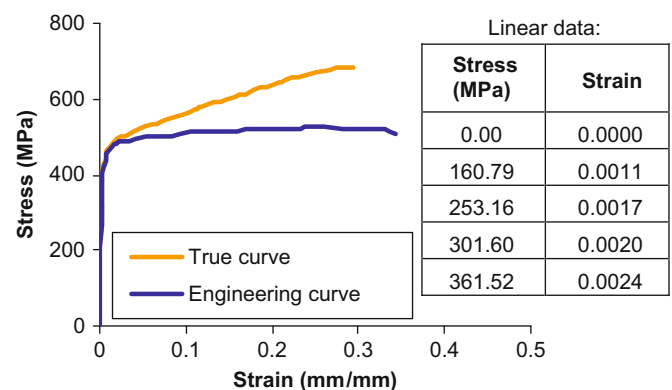
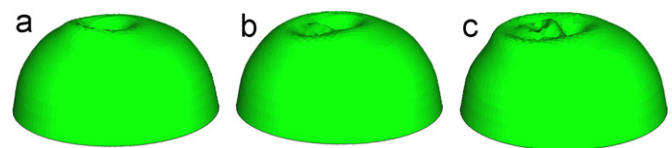| Linear data:	
Stress (MPa)	Strain
0.00	0.0000
160.79	0.0011
253.16	0.0017
301.60	0.0020
361.52	0.0024

Fig. 2. Stress–strain curves.

Fig. 3. Buckling mode shapes for specimen $D102–d25–t01–h48$: (a) first mode, (b) second mode, and (c) third mode.

Fig. 1. Cut view of specimens.

corresponding displacements were obtained. The effects of these mode shapes must be considered in a nonlinear buckling analysis (Static Riks step). Otherwise, the software may choose the buckling mode in an arbitrary manner and produce unrealistic results in nonlinear analyses. For the "buckle" step, the subspace solver method of the software was used. Due to the presence of contact constraints between the rigid plates and the shell, the Lanczos solver method cannot be used on these specimens [14]. In Fig. 3, three primary mode shapes are shown for the specimen D102–d25–t01.0–h48. After completion of the buckle analysis, a nonlinear analysis was performed to plot the load–displacement curve. This step is called "Static Riks" and uses the arc length method for post-buckling analysis. The nonlinearity of both material properties and geometry is taken into consideration in this analysis.

3. Loading by a rigid plate

In this section, the numerical results for D77–d25–h38, D53–d18–h28, and D102–d25–h48 specimens with thicknesses of 1.2, 1, 0.8, and 0.7 mm are analyzed. For comparison, the energy absorption capacity of specimens is a criterion that defines the mean collapse load. Mean collapse load is calculated by dividing the area under the load–displacement curve by the displacement of the upper rigid plate. The collapse is initiated by the formation of an axisymmetric ring at the smaller end during loading by a rigid plate. With further compression, the mechanism of collapse changes. At this stage, its propagation is due to the formation of an axisymmetric inward dimpling and a rolling plastic hinge

circle that is in contact with the top plate. Fig. 4 shows that the slope of the load–deformation curve changes appreciably.

As Fig. 5a and b show, the mean collapse load varies with the radius to thickness ratio for semi-spherical shells. This relationship exists after the shells are compressed 10 mm. It lasts until the absorber (semi-spherical) is entirely consumed and the apex of the semi-spherical shell makes contact with the rigid base plate. Fig. 5a shows that the mean collapse load decreases with an increase in the radius to thickness ratio (R/t ratio) of the spherical shell for the specimens of equal radii but of different thicknesses. The ratio decreases with an increase in the R/t ratio for specimens of equal thicknesses but of different radii. Fig. 5b shows that the mean collapse load decreases with an increase in the radius to thickness ratio (R/t ratio) of the spherical shell for the specimens of equal radius but of different thicknesses. However, the mean collapse load increases with an increase in the R/t ratio for the specimens of equal thicknesses but of different radii.

In a comparison of Fig. 5a and b, the best semi-spherical shell (the greatest mean collapse load) to be used in various height compression is a spherical shell with the maximum thickness and the minimum diameter.

4. Loading by different bars

In this section, the effect of loading conditions is considered. Therefore, some semi-spherical shells with a diameter equal to the small diameter of the spherical shells ($d=25$ mm) are loaded by a circular bar. Semi-spherical shells are also loaded by a square
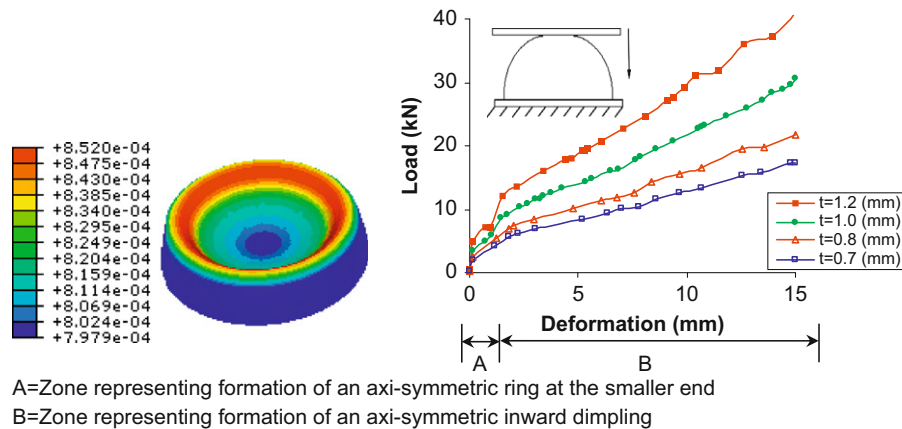

A=Zone representing formation of an axi-symmetric ring at the smaller end
B=Zone representing formation of an axi-symmetric inward dimpling

Fig. 4. Load-deformation curves of specimen D77–d25–h38 and wall thickness for a semi-spherical with thickness of 0.8 mm.
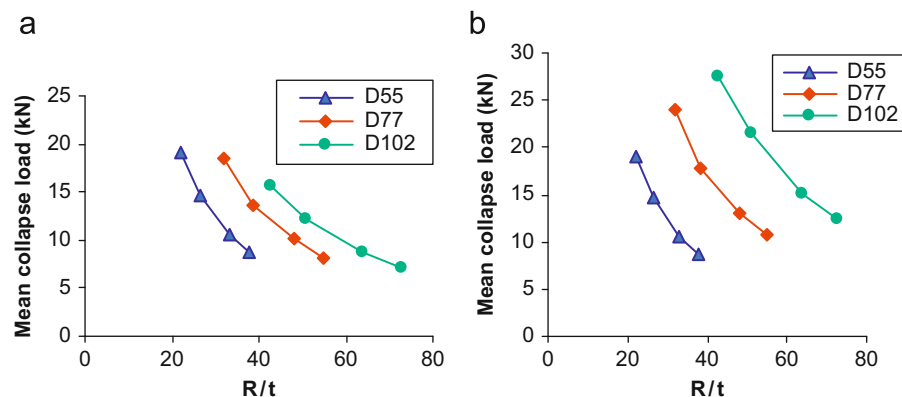

Fig. 5. Variation of mean collapse load vs. R/t values, (a) depth of deformation = 10 mm and (b) maximum depth of deformation.

bar with a side length equal to 22 mm. The cross-sectional area is equivalent to the two methods. Fig. 6 shows that a column with a semi-spherical end loads shells.

Fig. 7 illustrates the load-deformation curves that were obtained for the specimen D102–d25–t1–h48 with various loadings. During loading with a circular cross-section, only the first mode is observed from the formation of an axisymmetric ring towards inward dimpling. The formation of stationary plastic hinges and an integral number of 4 lobes were observed after loading with a square cross-section. This event occurred after the formation of an axisymmetric ring. However, formation of inward dimpling is not observed.

The primary part of the curve in loading by circular and square cross section bar is linear shown during a comparison of loading with a semi-spherical end shells with three other ones (rigid plate, circular column, and square column). Linear behavior is not observed in this type of loading. While loading with a semi-spherical column, the formation of an axisymmetric ring is not observed. A mode jump is observed with inward dimpling that leads to the formation of stationary plastic hinges and an integral number of 3 lobes.

Fig. 7 shows loading by a circular bar. The slope of the load deformation curve after the linear portion is comparable to the square bar. The absorption energy in the mode jump from the formation of an axisymmetric ring to inward dimpling is greater than the absorption energy in the mode jump from formation of an axisymmetric ring to lobe formation. In addition, the load–deformation curve for loading by a rigid bar with a semi-spherical cross section shows that the absorption energy decreases when the formation of an axisymmetric ring is eliminated.

Fig. 6. Loading with various bars, (a) circular cross section (CC), (b) square cross section (SC), and (c) spherical cross section (SPC).

Table 1 presents the results from a numerical analysis with the three different bars.

5. Loading by a rigid tube

In this section, the loading is carried out by a rigid 5 mm tube and a rigid plate with a hole. Fig. 8 shows the load–deformation curve and wall thickness of the specimen D102–d25–t0.8–h48, which has been loaded by the tube and a rigid plate with a hole and multiple θ values. A decrease in the value of θ corresponds to an increase in the mean collapse load. Fig. 9 shows the mean collapse load for the specimen D102–d25–t0.8–h48, which has been loaded by a rigid plate with a hole and a rigid tube. In comparison to loading with a rigid tube, Fig. 9 shows that the mean collapse load increases in loading by the rigid plate with a hole.

6. Loading by a rigid indentationed tube

In this section, the spherical shells are loaded with an indented tube. Four tubes with a 50 mm diameter and a thickness of 5 mm are chosen and indented (Fig. 10).
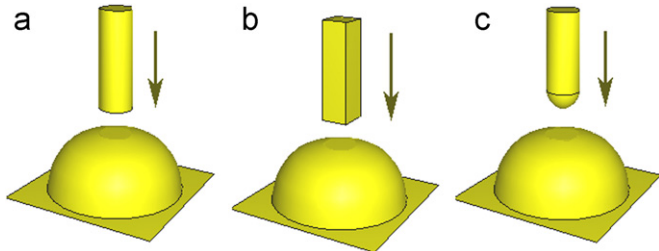
Table 1
Numerical analysis result for semi-spherical shells in loading by rigid bar with different cross sections.

| Specimens specification	Deformation height (mm)	Mean collapse load (kN)		
		SPC	SC	CC
D55–d18–t0.7–h28	25	3.6	4.2	4.2
D55–d18–t0.8–h28	25	4.3	5.1	5.2
D55–d18–t1.0–h28	25	6.0	7.1	7.3
D55–d18–t1.2–h28	25	7.8	9.4	9.8
D77–d25–t0.7–h38	35	4.0	4.7	5.0
D77–d25–t0.8–h38	35	4.9	5.8	6.1
D77–d25–t1.1–h38	35	6.7	8.1	8.5
D77–d25–t1.2–h38	35	8.6	10.4	11.1
D102–d25–t0.7–h48	40	3.8	4.4	4.7
D102–d25–t0.8–h48	40	4.9	5.4	5.7
D102–d25–t1.0–h48	40	6.8	7.8	8.1
D102–d25–t1.2–h48	40	9.1	10.4	10.6
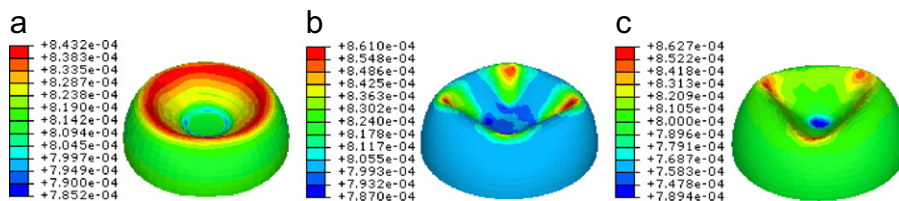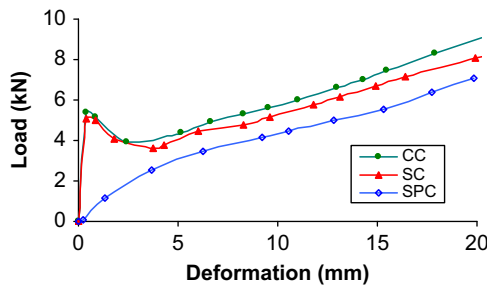
Fig. 7. Load-deformation curve for specimen D102–d25–t0.8–h48 and shell thickness in loading by, (a) circular cross section bar (CC), (b) square cross section bar (SC), and (c) spherical cross section bar (SPC).
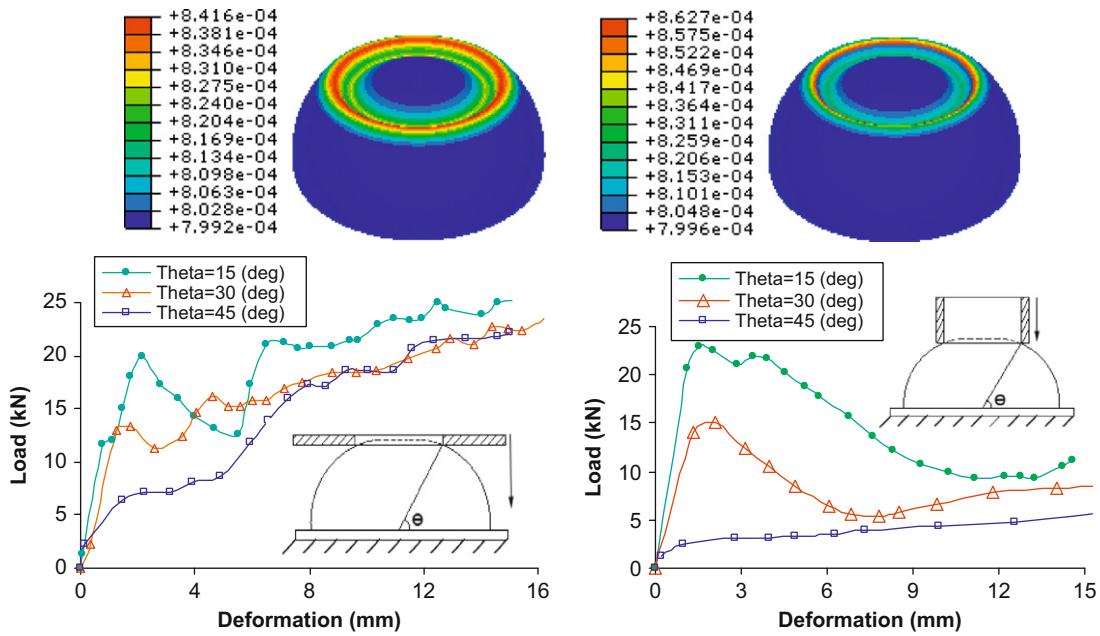
Fig. 8. Load-deformation curves and the wall thickness for the specimen $D102-d258-t0.8-h48$ at loading by rigid tube and rigid plate with a hole at $\theta = 60°$.
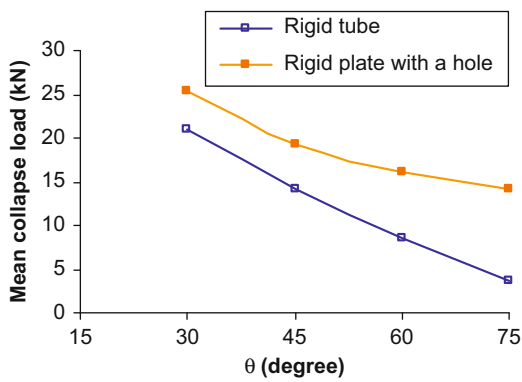

Fig. 9. Numerical analysis for semi-spherical shells in loading by rigid tube and rigid plate with a hole for specimen $D102-d25-t0.8-h48$.
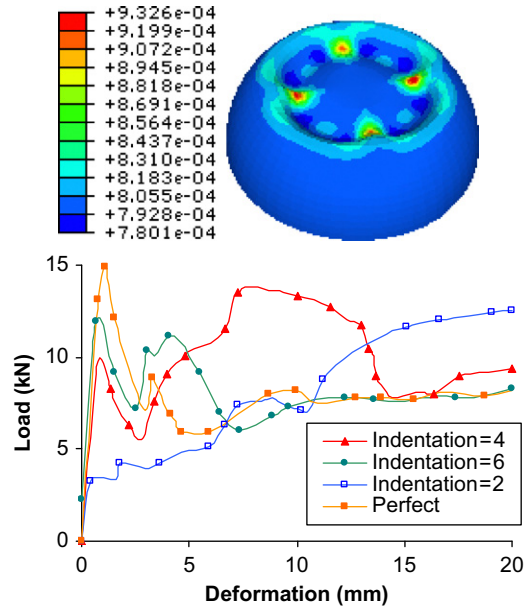

Fig. 11. Load-deformation curves and the wall thickness for the specimen $D77-d18-t0.8-h28$ in loading by rigid indented tubes.
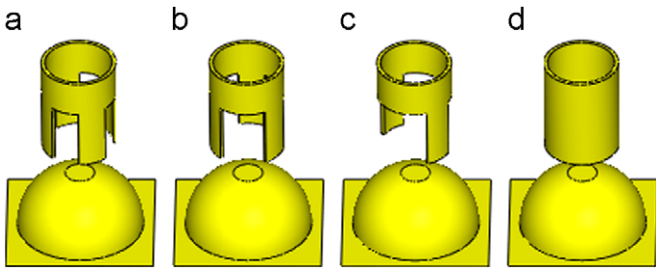

Fig. 10. Loading with indented tubes. (a) 2 indentation (2IN), (b) 3 indentation (3IN), (c) 4 indentation (4IN), and (d) perfect tube.

Fig. 12. Variation of mean collapse load with number of indentation for specimen $D77-d25-t0.8-h38$.

Fig. 11 shows the load–deformation curve and the wall thickness of $D77-d25-t0.8-h38$ in loading with different levels of indentation.

In Fig. 12, the mean collapse load curves are plotted against the number of indentations in the rigid tube. The mean collapse load increased with an increase in the number of indentations from 2
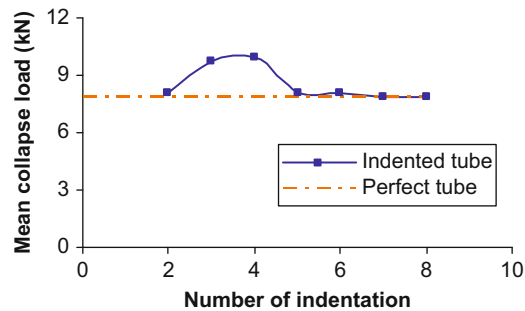
Fig. 13. A serve hydraulic INSTRON 8802 machine in loading on semi-spherical shell by circular bar.

to 4. The mean collapse load decreased with an increase in the number of indentations from 4 to 5. The collapse is constant with an increase in the number of indentations from 5 to 8. These observations indicate that with an increased number of indentations, the indented tube acted like a rigid tube.

7. Verification of numerical results with experimental results

Experimental tests were conducted on a large number of specimens in order to confirm the numerical results. For these tests, a servo-hydraulic INSTRON 8802 machine was used (Fig. 13).

The load deformation curves produced by numerical and experimental analyses are shown in Figs. 14–17. The mean collapse loads obtained from experimental and numerical studies are shown in Tables 2–5. Results indicate a minimal difference between the experimental and numerical results. For example, the average discrepancy between the two sets of results in Table 4 is 5% for the linear element and 3.6% for the S8R5
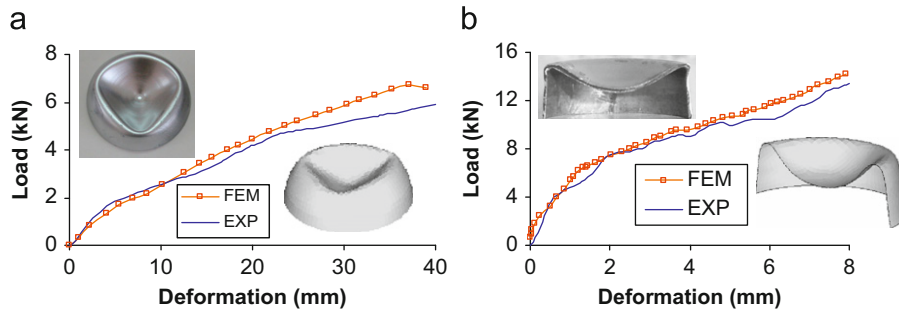

Fig. 14. Comparison of the experimental and numerical results for the specimen $D53-d18-t0.8-h28$ in loading with (a) rigid tube with semi-spherical cross section and (b) rigid plate.
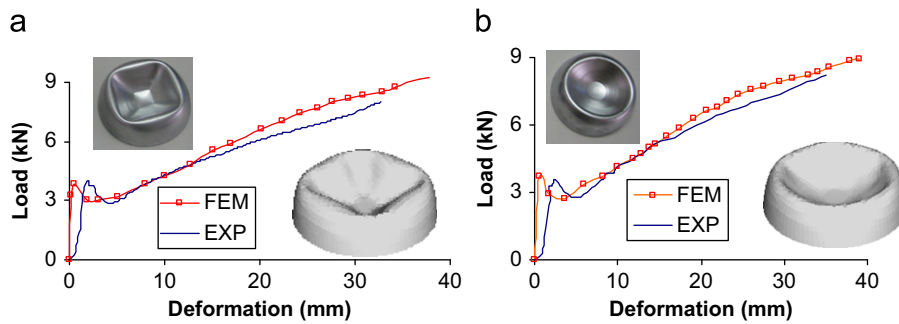

Fig. 15. Comparison of the experimental and numerical results for the specimen $D102-d25-t0.8-h48$ in loading by (a) square bar and (b) circular bar.
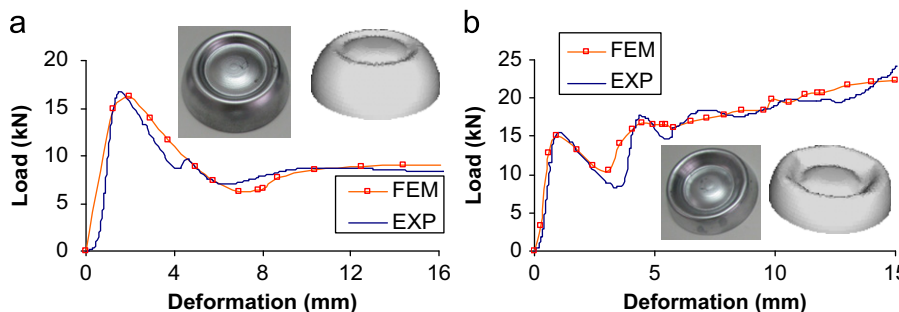

Fig. 16. Comparison of the experimental and numerical results for the specimen $D102-d25-t0.8-h48$ in loading by (a) rigid tube and (b) rigid plate with a hole.
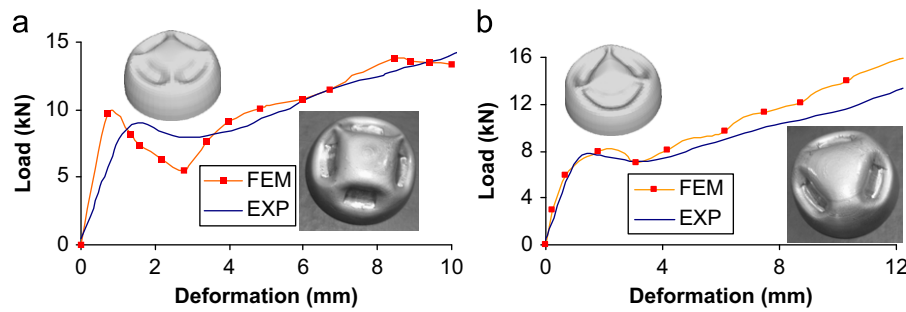
Fig. 17. Comparison of the experimental and numerical results for the specimen D77–d25–t0.8–h38 in loading by indented tube, (a) 4 indention and (b) 3 indention.

Table 2
Comparison of the experimental and numerical results for semi-spherical shells in loading with various bars.

Specimens specification	Deformation (mm)	Mean collapse load (kN) Numerical			Mean collapse load (kN) Experimental		
		SPC	CC	SC	SPC	CC	SC
D102–d25–t0.8–h48	35	4.6	5.5	5.2	4.3	5.2	5.0
D77–d25–t0.8–h38	30	4.9	6.1	5.8	4.6	5.7	5.3
D55–d18–t0.8–h38	20	4.0	5.0	4.8	3.9	4.7	4.6

The mean error is 5.5%.

Table 3
Comparison of the experimental and numerical results for specimen D102–d25–t0.8–h48 in loading with rigid tube and rigid plate with a hole.

Specimens specification	Vertical deformation (mm)	Mean collapse load (kN)		$|F_{NUM}-F_{EXP}|/F_{NUM} \times 100\%$
		Experimental	Numerical	
Rigid plate with a hole	15	16.5	17.4	5.4
Rigid tube	15	8.8	9.3	5.3

Table 4
Comparison of the experimental and numerical results for semi-spherical shells in loading with rigid plate.

Specimens specification	Vertical deformation (mm)	Mean collapse load (kN)			$|F_{NUM}-F_{EXP}|/F_{NUM} \times 100\%$	
		S4R element	S8R5 element	Experimental	S4R element	S8R5 element
D53–d18–t0.7–h28	8	7.3	7.2	6.8	5.8	4.4
D53–d18–t0.8–h28	8	9.2	9	8.7	5.3	3
D53–d18–t1.0–h28	8	12.2	12.3	11.7	4.2	4.6
D53–d18–t1.2–h28	8	16.3	16.1	15.4	5.7	4.7
D77–d25–t0.7–h38	12	8.8	8.6	8.4	4.6	1.9
D77–d25–t0.8–h38	12	10.9	10.8	10.5	3.9	2.7
D77–d25–t1.0–h38	12	14.1	14	13.2	6.4	5.6
D77–d25–t1.2–h38	12	19.9	19.6	19	4.1	3
D102–d25–t0.7–h48	20	10.3	10.1	9.7	5.6	3.6
D102–d25–t0.8–h48	20	12.6	12.5	11.8	5.9	5.3
D102–d25–t1.0–h48	20	18.7	18.4	17.6	5.9	4.4
D102–d25–t1.2–h48	20	24	23.4	23.3	3.1	0.6

The mean error is 5% for S4R element and 3.6% for S8R5 element.

Table 5
Comparison of the experimental and numerical results for semi-spherical shells in loading with indented tube.

Specimens specification	Number of indentation	Deformation height (mm)	Mean collapse load (kN)		$|F_{NUM}-F_{EXP}|/F_{NUM} \times 100\%$
			Experimental	Numerical	
D77–d25–t1–h38	3	10	8.0	9.0	11
D77–d25–t0.8–h38	4	10	9.6	10	4

nonlinear element. The results for nonlinear elements have fewer errors. The slope of the load vs. end-shortening curves is higher in the numerical results than in the experimental results before the buckling. This discrepancy is due to the presence of internal defects in the material. These defects reduce the stiffness of the specimens in the experimental method, whereas the numerical analyses assume the materials perform ideally.

8. Conclusion and discussion

In this paper, the behavior of buckling in thin-walled semi-spherical shells subjected to various loadings was studied. The buckling phenomenon plays an essential role in the load carrying capacity of the specimens. Fig. 18 shows that the energy–compression curves of the steel spherical shells that were subjected to loading by a rigid bar with a spherical cross section.

In conclusion, Fig. 18 indicates that absorbed energies follow a quadratic function. The difference between the absorbed energy for thicknesses of 0.7 and 0.8 mm with height compressions of 10, 20, 30, and 40 mm are 18.5%, 18.1%, 17.7%, and 18.4%, respectively. This result shows that the rate of increase remains approximately constant.

Fig. 7 shows a plot of the shell thicknesses in loading by a rigid bar. Loading with different bars shows that a maximum increase in thickness is obtained in stationary hinges; a minimum thickness is reached if it is in the contact zone of semi-spherical rigid bars.

Fig. 8 shows a contour plot of the shell thickness in loading by a rigid tube and a rigid plate with a hole. The maximum increase in thickness occurred in inner rolling plastic hinges.

The load–deformation and energy–compression curves obtained from tests conducted on spherical shells are presented in Figs.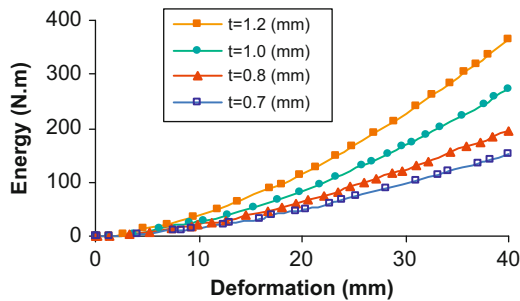 14–17. The shape of the load–deformation curve is an important characteristic of an energy absorber. An ideal energy absorber has a square wave load–deformation profile [15,16], i.e., once the buckling mode starts (at peak loads) the collapse continues under the same load until the absorber is entirely consumed. The load–deformation curves obtained from the loading by a rigid plate with a hole resemble that of an ideal energy absorber.

In Fig. 19, the experimental and numerical profiles of a semi-spherical tube have been shown after loading by a rigid plate. The experimental profiles were measured by filling the semi-spherical shell with paraffin at different stages of compression and by interrupting the axial compression of specimens in the INSTRON machine. As shown in Fig. 19, increases in the compression height leads to increases in the circumferential strain and a tending out of the semi-spherical shell.

In Table 6, rolling plastic hinges of semi-spherical with thicknesses of 1 and 0.8 mm have listed for specimens D77–d25–d38 and D102–d25–h48. Table 6 shows that a rolling plastic hinge increases with an increasing shell thickness and diameter. The difference between rolling plastic hinges in various thicknesses increases with an increase in the compression height.

The thickness of the shell changed due to the circumferential and meridional strain. Fig. 20 presented the wall thickness of the shell with a 15 mm compression. According to Fig. 20, the initial (nearly unstrained) flat region of the curve corresponds to the unreformed portion of the semi-spherical shell, which was minimally reduced. The reduction reached its maximum at the outer rolling plastic hinge due to stretching. The subsequent slope of the curve increased and reached its maximum at the inner rolling plastic hinge. A peak value, $\varepsilon_{th} = .077$, was predicted by a finite element analysis. After the peak value, the thickness strain decays because of progressive circumferential and meridional stretching.

Fig. 18. Energy–compression curves of specimens D102–d25–h48 in loading by rigid bar with spherical cross section.

Table 6
Comparison of rolling plastic hinge radius.

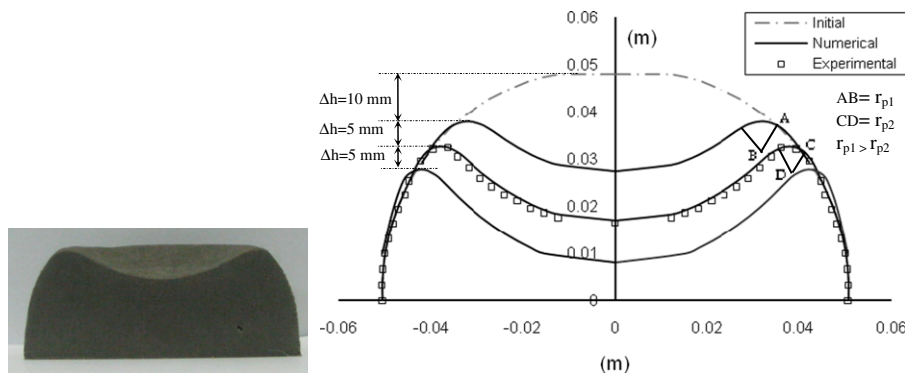| Compression height (mm)	Rolling plastic hinge radius (mm)			
	D102–d25–h48		D77–d25–h38	
	t = 0.8 mm	t = 1 mm	t = 0.8 mm	t = 1 mm
3	55.5	55.5	46.5	46.5
6	45	45	35	34.5
9	35.5	36	26	23.5
12	31	32	20	17
15	26.5	27.5	16	12
18	24	25	–	–
21	21	23	–	–
24	20	22	–	–

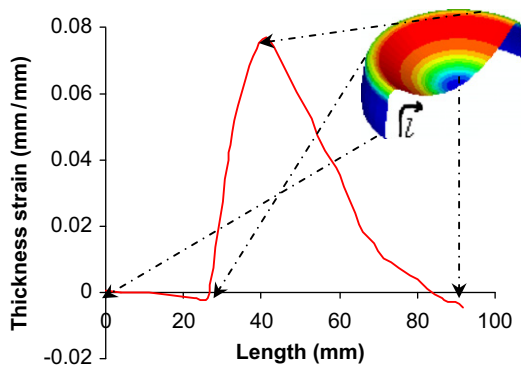**Fig. 19.** Measurement of deformed shapes at various stages.

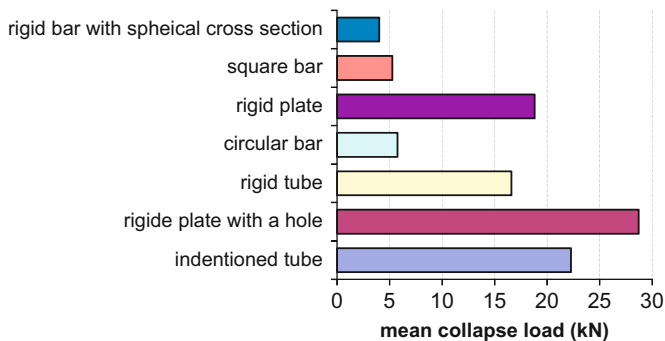**Fig. 20.** Distribution of the thickness strain along a cross-section of a semi-spherical ($D102$–$d25$–$t0.8$–$h48$).

Fig. 21. Summary of the results from the different loadings in terms of the mean collapse load for specimen $D77$–$d25$–$t0.8$–$h38$ at 10 mm compression.

Fig. 21 shows a synthesis of the mean collapse load and various loading. The mean collapse load is a good indicator of the energy absorption capability. The rigid plate with a hole is the more efficient solution for energy absorption.

9. Concluding remarks

Semi-spherical shells of different loading were investigated experimentally and numerically. The load–deformation projections at different stages of compressions match well with results obtained from experiments. The predicted deformed shapes at different stages of compressions and various loadings correspond well with the actual deformed profiles. The following results were found in this study:

1. The mean collapse load is greater with loading by circular bar compared to loading with a square bar or a rigid bar with a spherical cross section. When compared to the two other types of bars, the mean collapse load is less for loading by a rigid bar with a spherical cross section.

2. The mean collapse load is greater for loading by a rigid plate with a hole than for a loading by a rigid tube. The mean collapse load increases with an increase in the whole diameter of the rigid tube and plate.

3. In loading with an indented tube, the tube with 4 indentations has the highest mean collapse load value.

4. The thickness of a shell changes during compression. The thickness strain is greater for stationery plastic hinges when compared to rolling plastic hinges.

5. Rolling plastic hinges increase with an increase in shell thickness and diameter.

6. The best semi-spherical shell (with a maximum mean collapse load) for various height compressions is one with the maximum thickness and the minimum diameter.

7. The shell can tolerate a greater mean collapse load when it is loaded by a rigid plate with a hole than it can when it is loaded with a rigid plate, bar, or tube.

References

[1] Lekie FA, Penny PK. Plastic instability of a spherical shell. In: Heyman J, Leckie FA, editors. Engineering Plasticity. 1968, p. 401–11.

[2] Morris A, Calladine CR. The local strength of thin spherical shell loaded radially through a rigid boss. In: Berman I, editor. Proceeding of the first international conference on pressure vessel technology. 1969. p. 35–44.

[3] Updike DP. On the large deformation of a rigid plastic spherical shell compressed by a rigid plate. Journal of Engineering for Industry 1972;94:949–55.

[4] Kitching R, Houston R, Johnson W. A theoretical and experimental study of hemispherical shells subjected to axial loads between flat plates. International Journal of Mechanical Sciences 1975;17:693–703.

[5] De'Oliveria JG, Wierzbicki T. Crushing analysis of rotationally symmetric plastic shells. Journal of Strain Analysis 1982;17(4):229–36.

[6] Kinkead AN, Jennings A, Newell J, Leinster JC. Spherical shells in inelastic collision with a rigid wall tentative analysis and recent quasi-static testing. Journal of Strain Analysis 1994;29(1):17–41.

[7] Gupta NK, Eswara Prasad GL, Gupta SK. Axial compression of metallic spherical shells between rigid plates. International Journal of Thin-Walled Structures 1999;34(1):21–41.

[8] Gupta NK, Venkatesh G. Experimental and numerical studies of dynamic axial compression of thin walled spherical shells. International Journal of Impact Engineering 2004;30(8–9):1225–40.

[9] Gupta PK, Gupta NK. A study of axial compression of metallic hemispherical domes. Journal of Materials Processing Technology 2009;209:2175–9.

[10] Ruan HH, Gao ZY, Yu TX. Crushing of thin-walled spheres and sphere arrays. International Journal of Mechanical Sciences 2006;48:117–33.

[11] Alghamdi AAA. Collapsible impact energy absorbers: an overview. Thin-Walled Structures 2001;39:189–213.

[12] ASTM A370-05, Standard test methods and definitions for mechanical testing of steel products.

[13] ABAQUS 6.7 PR11 user's manual.

[14] Shariati M, Rokhi MM. Numerical and experimental investigations on buckling of steel cylindrical shells with elliptical cutout subject to axial compression. Thin Walled Structures 2008;46(11):1251–61.

[15] Gupta NK, Mohamed Sheriff N, Velmurugan R. Experimental and numerical studies of buckling of thin spherical shells under axial loads. International Journal of Mechanical Sciences 2008;50:422–32.

[16] Gupta NK, Mohamed Sheriff N, Velmurugan R. Experimental and numerical investigations into collapse behavior of thin spherical shells under drop hammer impact. International Journal of Solids and Structures 2007;44:3136–55.